Editors' Suggestion

Probing the exciton spin-valley depolarization with spin-momentum-valley locked unbound states using tr-ARPES

Mehdi Arfaoui,[1,2,*] Robson Ferreira,[1,†] and Sihem Jaziri[2,3]
[1]*Laboratoire de Physique de l'École Normale Supérieure, ENS, Université PSL, CNRS, Sorbonne Université, Sorbonne Paris Cité, Paris, France*
[2]*Laboratoire de Physique de la Matière Condensée, Département de Physique, Faculté des Sciences de Tunis, Université Tunis El Manar, Campus Universitaire 1060 Tunis, Tunisia*
[3]*Laboratoire de Physique des Matériaux Structure et Propriétés, Faculté des Sciences de Bizerte, Université de Carthage, 7021 Jarzouna, Tunisie*

(Received 25 June 2024; accepted 4 October 2024; published 5 December 2024)

Time-resolved, angle-resolved photoemission spectroscopy (tr-ARPES) is a powerful technique to access the ultrafast dynamics of intervalley couplings and population exchanges. In monolayer transition metal dichalcogenides, this is advantageous due to the fact that excitons have a large binding energy, allowing them to be resonantly excited by a short-pulse pump without also putting into play a large set of dissociated electron-hole pairs, while at the same time remaining relatively localized in momentum space so that the outgoing currents related to different local valleys can be safely distinguished in the energy-momentum resolved tr-ARPES signal. In this work, we present a detailed theoretical description of the high-energy states that form the escape continuum for photoejected electrons in a tr-ARPES experiment, paying particular attention to their momentum dispersions, time-reversal symmetries, and spin characteristics. The analysis of the various symmetries fulfilled by such unbound states reveals the existence of a momentum-valley locking for the unbound final electron states, sharing various features with the valley Hall effect. Moreover, the photoextracted current under a circularly polarized pump ideally presents a robust triple locking of momentum direction, valley origin, and spin orientation, which permits envisioning an on-demand source of highly spin-polarized electrons on vacuum. We also present a study of the robustness of such findings against intervalley processes that tend to mitigate the valley-spin polarization of the intermediate exciton states. To further investigate this aspect, we consider in detail the role of Coulomb-exchange driven intervalley coupling. That allows us to quantify the dependence of the tr-ARPES measurements upon various setup parameters, such as the incident angle and light helicity. Finally, we present a critical discussion about the role of a few intervalley couplings and/or scattering processes. Our findings have broad implications and are anticipated to be applicable to other two-dimensional structures and intervalley scattering events.

DOI: 10.1103/PhysRevResearch.6.043243

I. INTRODUCTION

Monolayer transition metal dichalcogenides (ML-TMDs), which are materials characterized by the chemical formula MX_2 (where M is a transition metal and X is a chalcogen atom, M = Mo, W; X = S, Se), have attracted intense interest in recent decades [1–3]. They show semiconductor characteristics with a direct band gap in the near-infrared spectral region, involving two energy-degenerate interband transitions at the two nonequivalent vertices (which we denote $\mathbf{K}_{(\pm)}$ in the following) of their hexagonal Brillouin zone (BZ) [4]. The concomitance of a sizable spin-orbit coupling and the absence of spatial centrosymmetry is at the origin of a series of specific, time-reversal related properties involving the TMD valence and conduction states, among which are the spin-valley locking (SVL) and the valley Hall effect (VHE) [5–9]. The SVL results in the possibility to optically excite carriers at only one of the valleys by using circularly polarized light (optical-valley selectivity effect), and it has been largely studied in the literature [10–12]. The VHE consists of a lateral deviation (with respect to the applied bias axis) along opposite directions for conducting carriers in opposite valleys, which has also been recently demonstrated experimentally [7,8]. Both effects involve states around the fundamental band gap, and they rely on the nonequivalence of the $\mathbf{K}_{(\pm)}$ valleys. To the best of our knowledge, effects discriminating between time-reversal symmetry in higher-energy bands as well as vacuum states have so far not been discussed in the literature.

Excitons play a crucial role in TMDs. The coexistence of a complex single-particle band structure, characterized by various energetically near valleys and important spin-orbit related effects, with a strong Coulomb electron-hole (e-h) coupling, gives rise to a rich set of excitonic states [13–17]. In fact,

*Contact author: mehdi.arfaoui@fst.utm.tn
†Contact author: robson.ferreira@ens.fr

compared to conventional semiconductors, the confinement into a single layer, the reduced dielectric screening, and the heavier electron and hole effective masses contribute to the strengthening of the Coulomb interactions, and eventually to the formation of a robust (against temperature dissociation) fundamental exciton state with a small Bohr radius $\sim$ a few nm and a large binding energy on the order of hundreds of meV [3,16–21]. Moreover, the interacting electron and hole may pertain to different valleys, generating strongly correlated but momentum-forbidden (with regard to dipolar optical transitions) states. The *e-h* correlations, as measured by the exciton binding energies, are very often superior to spin-orbit splitting of the conduction and valence bands. In the same way, the Coulombic coupling admixes single carrier states spread over an important fraction of the BZ (typically of the size of the Bohr radius inverse). A related question that is still not completely settled is whether the photogenerated excitons have a predominant valley assignment, and to what extent is this SVL property robust. In fact, the first optical experiments used to demonstrate the optical-valley selectivity in undoped samples were often analyzed in terms of exciton transitions. In the same way, earlier descriptions of exciton states were done within the *Wannier-Mott* model, which treats separately excitons pertaining to different valleys [22,23]. Such studies, which support a SVL for excitons, launched the field of valleytronics, the applications of which actually rely on the existence of long ($\sim$ nanoseconds or greater) valley lifetimes, where the carrier imbalance created by selective pumping of $\mathbf{K}_{(+)}$ or $\mathbf{K}_{(-)}$ lasts long enough for gate operations to be performed [5,6,11,24]. However, more recent investigations point out the existence of an ultrafast sub- to few-picosecond valley depolarization [25–28]. It turns out that an efficient valley depolarization can be triggered by different processes, either intrinsic (related to the following intervalley Coulomb-mediated couplings: the *e-h* exchange interaction [25], a Dexter-like mechanism [29], and multiexciton contributions [30]) or extrinsic (intervalley scattering by defects [31] or phonons [32,33]). The vast majority of the studies rely on quasiresonant (i.e., around the fundamental band gap) optical experiments, using either one-color or two-color excitations.

The exciton-valley depolarization may alternatively be directly probed by time-resolved and angle-resolved photoemission spectroscopy (tr-ARPES) experiments. Exchange-related coupling leads to the formation of stationary intervalley exciton states with no clear valley signature [34,35]. The latter coupling affects only propagating excitons, i.e., with nonvanishing center-of-mass (COM) wave vector $\mathbf{K}_{\mathrm{CMX}}$, as referenced to a valley extremum like the ones generated inside the light cone by an oblique photoexcitation. This has been predicted to lead to efficient exciton valley depolarization [10,34,36]. However, the latter coherent stationary picture may be strongly affected by incoherent intravalley scatterings that alter $\mathbf{K}_{\mathrm{CMX}}$ during the radiative recombination (exciton radiative lifetimes ranging from a few picoseconds at 4 K [36,37] to a few nanoseconds at room temperature [36] have been reported). As reported in some works, such scatterings may considerably inhibit the valley depolarization, similarly to the strong inhibition of the spin-depolarization measured for independent carriers and excitons in semiconductor quantum wells in the frequent spin-conserving collisions regime, and described by the D'Yakonov-Perel mechanism [38,39]. As a consequence, the valley-depolarization rate extracted from time-resolved optical experiments may not give a direct measure of the coherent intervalley coupling in the general case, but it appears to be a sample-quality-dependent quantity.

The tr-ARPES technique results are well suited to the study of exciton states in TMDs, as reported in different theoretical [12,40–45] and experimental [46–50] works. In the experiments, the electron of the exciton photogenerated by the pump pulse is extracted out of the TMD layer by a delayed probe pulse, injected into the vacuum continuum, and then collected by the analyzer, which measures its momentum and energy with good accuracy (see, e.g., [51–53] for more details). Recent measurements clearly demonstrate that excitons sit energetically below the interband continuum edge, and they are essentially formed out of one-electron states dispersed in the reciprocal space around the six corners (the $K_{(\pm)}$ edges) of the first BZ, in agreement with predictions. However, calculations and experiments were performed for a restricted set of pump and probe excitation parameters of the two pulses, and without paying enough attention to the tight relationship between the final escape states and the TMD band structure. Notably, the roles of the incidence angle, the polar angle, and the polarization state of the two pulses were not analyzed in full detail. We present below a more detailed analysis of exciton-mediated tr-ARPES. We pinpoint the importance of a careful description of the final states (in particular of their time-reversed characteristics), and we show that the vacuum photocurrent signal can be highly modulated by playing with the pump characteristics. Strikingly, we find that the photoejected electrons carry outside the TMD layer the "internal" spin-valley selectivity of $K_{(\pm)}$ states, namely that electrons of opposite spins, extracted from excitons photocreated in different valleys, propagate along different directions in a vacuum, and that an on-demand 100% spin-polarized current can in principle be generated and controlled by the pump polarization under normal incidence. We additionally describe a protocol to obtain direct information on the exciton fine structure governed by the intervalley coupling, using an oblique incidence pump excitation and a variable pump-probe delay T_2. It relies on the ability of the probe pulse to extract the electron from the exciton in a time T_2 that is shorter than typical scattering times, but that can be a significant fraction of the one for a coherent valley-flip process under the action of the intervalley coupling.

The paper is organized as follows. In Sec. II, we review the model calculation of the photoelectron current in the framework of a second-order perturbation theory, and we apply it to the case of arbitrary incidence angle and optical pulses polarizations, and to exciton states described within the N-electron formalism. We also present our description of the high-energy states that form the escape continuum for photoejected electrons, paying particular attention to their momentum dispersions and time-reversal symmetries. In fact, electrons extracted from exciton states near one of the $K_{(\pm)}$ edges necessarily occupy continuum states with total in-plane wave vector near the same edge, due to the fact that both the pump and probe pulse wave vectors are sizeably smaller than the BZ size. In Sec. III, we consider the consequences of the various symmetries and approximations on the details of the

tr-ARPES signal. We stress the existence of a momentum-valley locking for the unbound final electron states, and we develop its similarity with the VHE. We also discuss the spin characteristics of the photoextracted current, and we show that the latter ideally presents a robust triple locking of momentum direction, valley, and spin orientation. Section IV is devoted to the consideration of intervalley exchange effects. We investigate in detail how this coherent coupling modifies the exciton states and therefore influences the ARPES signal. We show in particular that the triple-locking property of the photocurrent can be monitored on demand by playing with the pump and probe pulse characteristics. Various polarization configurations are considered, and the role of the incidence angle and delay time T_2 is discussed for each case. We also present a protocol to extract information on the internal exciton spin-valley depolarization from the ARPES measurements. Finally, Sec. V presents a critical discussion of the role of various forms of intravalley and intervalley couplings and scattering processes (particularly phonon-related ones) on the ARPES signal, and the possible utilization of the latter technique to access the dynamics of intervalley processes in a monolayer TMD.

II. MODEL OF TR-ARPES AND ELECTRONIC STATES

The exciton-mediated tr-ARPES photoemission has been modeled in a few works [40–43,45]. In the time-evolution framework, the photoejection probability into a final $|f\rangle$ state is given by $P_f = |A_f|^2$, where A_f is the second-order probability amplitude:

$$A_f \approx \sum_{\nu} C_{f,\nu}(T_2)\, \hat{\boldsymbol{\epsilon}}_2 \cdot (\boldsymbol{\Pi}_{2N})^{f}_{\nu}\, \hat{\boldsymbol{\epsilon}}_1 \cdot (\boldsymbol{\Pi}_{1N})^{\nu}_{\emptyset}, \quad \text{(1a)}$$

$$C_{f,\nu}(T_2) = r_0^2\, I_{\omega_f,\omega_\nu}(T_2)\, e^{-i\omega_{\nu,\emptyset}T_2}, \quad \text{(1b)}$$

where $r_0 = -ie/\hbar m_0$, and m_0 is the free-electron mass. We note $(\boldsymbol{\Pi}_{nN})^{B}_{A} = \langle A|[\exp(i\mathbf{q}_n \cdot \mathbf{r})\mathbf{p}]_N|B\rangle$ is a matrix-element between two N-electron (Slater) states $|A\rangle$ and $|B\rangle$, where $[\exp(i\mathbf{q}_n \cdot \mathbf{r})\mathbf{p}]_N = \sum_{j=1}^{N} \exp(i\mathbf{q}_n \cdot \mathbf{r}_j)\mathbf{p}_j$, and $\mathbf{r}_j$ and $\mathbf{p}_j$ are, respectively, the position and momentum of the jth electron. We also define $(\boldsymbol{\Pi}_n)^{b}_{a} = \langle a|\exp(i\mathbf{q}_n \cdot \mathbf{r})\mathbf{p}|b\rangle$ as the usual matrix element between one-electron states $|a\rangle$ and $|b\rangle$. $|\emptyset\rangle$ is the ground crystal state; $|f\rangle$ is the final state (to be better characterized later on) with an outgoing free electron and one remaining hole in the valence band of the TMD layer; and labels $n =$ "1" and $n =$ "2" hold for the near-infrared (NIR) pump and the high-energy extreme ultraviolet (XUV) probe pulses, respectively, of polarization $\hat{\boldsymbol{\epsilon}}_n$, average pulsation ω_n, and wave vector $\mathbf{q}_n$, temporally separated by delay T_2. Taking Oz as the axis perpendicular to the TMD plane, one has $\hat{\boldsymbol{\epsilon}}_n = (\boldsymbol{\epsilon}_{n\parallel}, \boldsymbol{\epsilon}_{nz})$ and $\hat{\mathbf{q}}_n = (\mathbf{q}_{n\parallel}, \mathbf{q}_{nz})$, with $\parallel$ indicating in-plane component. The sum is performed over all intermediate exciton states $|\nu\rangle$ that can be photoexcited by the pump. A_f (and thus P_f) is evaluated for times far after the probe pulse, and is then time-independent. Finally, $I_{\omega_f,\omega_\nu}(T_2)$ is a delay-dependent function that reduces to the product $\tilde{A}_2(\delta\omega_{2\nu})\tilde{A}_1(\delta\omega_{1\nu})$ when the two pulses do not overlap (i.e., when T_2 is much larger than the pulse widths), where $\tilde{A}_n(\omega) = \int_{-\infty}^{\infty} d\tau \cos(\omega\tau)A_n(\tau)$ contains all information on the temporal profiles $A_n(\tau)$ of the potential vectors, and on the excitation detunings $\delta\omega_{2\nu} = \omega_f - \omega_\nu - \omega_2$ and $\delta\omega_{1\nu} = \omega_\nu - \omega_\emptyset - \omega_1$. We will not reproduce the short-delay expression for $I_{\omega_f,\omega_\nu}(T_2)$, which can be found, e.g., in [40].

Let us first focus on the states associated with the direct fundamental interband transition of an ML-MX_2 system, which can be excited by the pump pulse. The band gap occurs at the $\mathbf{K}_{(\tau)}$ vertices of the hexagonal two-dimensional (2D) BZ, where $\tau = \pm 1$ is the valley label. Recall that the $\mathbf{K}_{(\tau)}$ valleys are each at the confluence of three BZs, and occupy in the repeated zone representation the $\mathbf{k}$-space regions near the vectors $\mathbf{K}_{(\tau)} = \tau\mathbf{K}_0$ [colored regions in Fig. 1(a)]. We denote $|B, \tau\rangle$ the state of the B band at the $\mathbf{K}_{(\tau)}$ point of the BZ: $B = v(c)$ for the topmost (lower-lying) one-electron valence (conduction) state that defines the fundamental band gap of the valley τ (the high-energy bands involved in the photoejection process will be discussed later). We denote correspondingly $|B, \mathbf{k}, \tau\rangle$ as a state near the band B extremum of $\mathbf{K}_{(\tau)}$ valley, which possesses a total wave vector $\mathbf{k} + \mathbf{K}_{(\tau)}$ ($|\mathbf{k}| \ll |\mathbf{K}_{(\tau)}| = K_0 = 4\pi/3a_0$, where a_0 is the lattice constant). We also mention that the interband matrix elements $\langle c, \tau|\mathbf{p}|v, \tau\rangle$ can be written as $\langle c, \tau|\mathbf{p}|v, \tau\rangle = \Pi_{(\tau)} \cdot \hat{\boldsymbol{\sigma}}^{*}_{(\tau)}$, where $\hat{\boldsymbol{\sigma}}_{(\pm)} = (\hat{\mathbf{x}} \pm i\hat{\mathbf{y}})/\sqrt{2}$ forms an in-plane orthogonal basis ($\hat{\boldsymbol{\sigma}}_{(\alpha)} \cdot \hat{\boldsymbol{\sigma}}_{(\beta)} = 1 - \delta_{\alpha,\beta}; \hat{\boldsymbol{\sigma}}_{(\alpha)} \cdot \hat{\boldsymbol{\sigma}}^{*}_{(\beta)} = \delta_{\alpha,\beta}$). This form directly expresses the SVL effect (see below). Moreover, $\Pi_{(-)} = -(\Pi_{(+)})^{*}$, due to the time-reversal relation between states of the two valleys.

An interband optical excitation generates an e-h pair, which interact to form an exciton. The e-h Coulombic coupling has both a direct and an exchange component. Let us consider initially the first term and leave the second one to Sec. IV. The direct term is valley-diagonal and leads to independent *Wannier-Mott* excitons associated with either valley, as discussed in many papers [35,54]. We restrict here our discussion to excitons related to the fundamental interband transition (A-exciton), and we use the envelope function approximation to describe them. S-symmetry states are the only ones with nonvanishing dipolar coupling to light. We denote $|\nu\rangle \to |nS, \mathbf{K}_{\mathrm{CMX}}; \tau_X\rangle$ the nth S-like state with e-h 2D reduced motion $\varphi_{nS}(\boldsymbol{\rho})$, free COM wave vector $\mathbf{K}_{\mathrm{CMX}} = \mathbf{k}_e - \mathbf{k}_h$, where $\mathbf{k}_e$ ($\mathbf{k}_h$) is the wave vector of the electron (hole), and pertaining to the τ_X valley. Note that the exciton envelope function $\varphi_{nS}(\boldsymbol{\rho})$ is purely 2D, while $|v, \tau\rangle$ and $|c, \tau\rangle$ are formed out of 3D atomic orbitals. We have approximately

$$(\boldsymbol{\Pi}_{1N})^{|nS,\mathbf{K}_{\mathrm{CMX}};\tau_X\rangle}_{|\emptyset\rangle} \approx \delta_{\mathbf{K}_{\mathrm{CMX}}-\mathbf{q}_{1\parallel}} \sqrt{S}\, \varphi^{*}_{nS}(0)\, \hat{\boldsymbol{\sigma}}^{*}_{(\tau_X)} \Pi_{(\tau_X)}. \quad (2)$$

The matrix elements $\langle c, \mathbf{k} + \mathbf{K}_{\mathrm{CMX}}; \tau|\exp(i\mathbf{q}_1 \cdot \mathbf{r})\mathbf{p}|v, \mathbf{k}; \tau\rangle \approx \boldsymbol{\Pi}_{(\tau)}$ were evaluated in the dipole approximation ($\mathbf{q}_1 \to \mathbf{0}$) and using the $\mathbf{K}_{(\tau)}$ extremum wave functions $|B, \tau\rangle$. The Kronecker delta $\delta_{\mathbf{K}_{\mathrm{CMX}}-\mathbf{q}_{1\parallel}}$ reflects the in-plane translation invariance. Note also that the oscillator strength (per unit surface) of the nS exciton is proportional to $|\varphi^{*}_{nS}(0)\Pi_{(\tau_X=\pm)}|^2$. Equation (2) reflects the valley selectivity (the SVL) for the NIR pump: an $\hat{\boldsymbol{\epsilon}}_1 = \hat{\boldsymbol{\sigma}}_{(\tau_1)}$ excitation generates excitons only at the $\tau_X = \tau_1$ valley. For arbitrary pump polarization, $\hat{\boldsymbol{\epsilon}}_1 \cdot \hat{\boldsymbol{\sigma}}^{*}_{(\tau_X)}$ should not vanish to generate excitons at the valley τ_X.

The probe pulse breaks the exciton entity by promoting its electron into a continuum of high-energy states. Let us consider such states. One often uses two approximations to describe them: the final-state Coulombic interaction with the remaining hole is neglected, and the outgoing state is

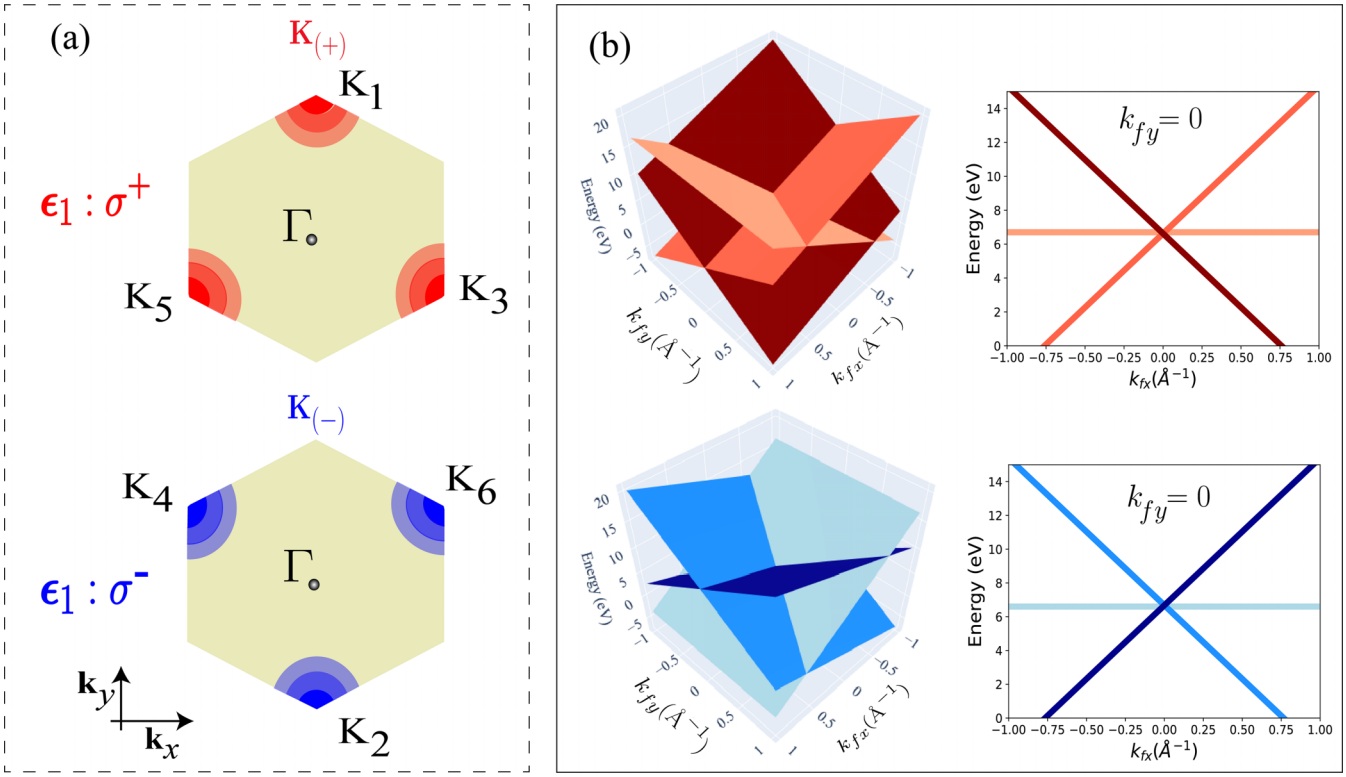

FIG. 1. (a) Scheme of the hexagonal BZ and the regions (colored in red and blue) around the nonequivalent vertices that define the $\mathbf{K}_{(+)}$ and $\mathbf{K}_{(-)}$ valleys in the repeated zone representation. The reciprocal-lattice vectors link the three equivalent corners that define the $\mathbf{K}_{(+)}$ edge. (b) Scheme of the triple in-plane dispersion for fixed $k_{fz} = 0$ and for a given lattice constant $a_0 = 3.17$ Å (e.g., for MoS_2) and their projection at $k_{fy} = 0$ of free-electron states around a $\mathbf{K}$-edge of the BZ, probed after being circularly polarized by pump excitation $\hat{\boldsymbol{\sigma}}_{(+)}$ (upper panel) and $\hat{\boldsymbol{\sigma}}_{(-)}$ (lower panel).

modeled by a plane wave [55–57]. In addition, as shown below in Eq. (3), the final in-plane wave vector sits near a $\mathbf{K}$-edge. In the repeated zone representation, the wave vectors for the available final states near the $\mathbf{K}_{(\tau_f)}$ edge read $\mathbf{k}_f + \mathbf{K}_{(\tau_f)} + \tau_f \mathbf{a}_{(j)}$, with $j = 1, 2, 3$, and $\mathbf{a}_{(1)} = 0$ and $\mathbf{a}_{(2,3)}$ are the two BZ wave vectors that link $\mathbf{K}_{(+1)}$ to its two equivalent vertices [see Fig. 1(a)]. $\mathbf{k}_f = (\mathbf{k}_{f\parallel}, k_{fz})$ is the propagation wave vector, with $\mathbf{k}_{f\parallel}$ a small in-plane displacement from the $\mathbf{K}$-edge ($|\mathbf{k}_{f\parallel}| \ll K_0$), and $\mathbf{k}_{fz}$ accounts for the outgoing motion of the free electron perpendicular to the TMD layer. We note in the following $\mathbf{K}_{(\tau,j)} \equiv \mathbf{K}_{(\tau)} + \tau \mathbf{a}_{(j)}$ the wave-vector positions of the three equivalent vertices that form the $\mathbf{K}_{(\tau)}$ valley, which have the same norm $|\mathbf{K}_{(\tau,j)}| = K_0$ but point along 120°-rotated directions in the TMD plane. Of course, $\mathbf{K}_{(-\tau,j)} \equiv -\mathbf{K}_{(+\tau,j)}$ form another set of three vectors, 60°-rotated with respect to the previous ones. In the end, the final free-electron states read $|\mathbf{k}_{f\parallel}, k_{fz}; \tau_f, j_f\rangle$. The band label j_f plays a similar role to B for the bound dispersions, while k_{fz} is specific to the 3D final states. The outgoing electron has total momentum $\mathbf{p}_f = \hbar(\mathbf{k}_f + \mathbf{K}_{(\tau_f, j_f)})$ and energy $E_f = \mathbf{p}_f^2/2m_0$. The energy dispersions of a free electron are thus approximately given by $E_{f,\tau,j} \approx \hbar^2(\mathbf{K}_0^2 + k_{fz}^2)/2m_0 + (\hbar^2/m_0)\mathbf{K}_{(\tau,j)} \cdot \mathbf{k}_{f\parallel}$ and form for a fixed k_{fz} a set of three intercrossing surfaces (roughly planes) in $\mathbf{k}$-space near each $\mathbf{K}$ edge; see Fig. 1(b). For a given valley, each planar dispersion corresponds thus to a roughly constant in-plane velocity $\mathbf{v}_{f\parallel,\tau,j} = (1/\hbar)\partial E/\partial \mathbf{k}_{f\parallel} \approx (\hbar/m_0)\mathbf{K}_{(\tau,j)}$ of the same absolute value but directed along the directions of the three equivalent BZ vertices of the given valley. For comparison, the energy dispersions of the bound ($B = v, c$) states are roughly quadratic around the $\mathbf{K}$-edges and correspond to much smaller velocities (they actually vanish at the $\mathbf{K}$-edges). The three intercrossing quasiplanar free dispersions of a $\mathbf{K}$ valley are schematically presented in Fig. 1(b).

The final states pertinent for the photoemission process correspond to a dissociated e-h pair with the in-plane COM wave vector $\mathbf{K}_{\mathrm{CM}f}$ (because of the in-plane translation invariance of the problem) and a vacancy (a hole in the valence band) with 2D wave vector $\mathbf{k}_{hf}$. We write $|c_f; \tau_f\rangle = |\mathbf{k}_{hf} + \mathbf{K}_{\mathrm{CM}f}, k_{fz}; \tau_f, j_f\rangle$ for the final electron and $|v_f; \tau_f\rangle = |v, \mathbf{k}_{hf}; \tau_f\rangle$ for the final hole states. Note that they are both near the same $\mathbf{K}_{(\tau_f)}$ point of the BZ, as will become clear below. For the independent e-h pair $|c_f; \tau_f\rangle \otimes |v_f; \tau_f\rangle$ in the final state, the probe contribution in Eq. (1) reads

$$(\boldsymbol{\Pi}_2)^{|f\rangle}_{|nS,\mathbf{K}_{\mathrm{CM}X};\tau_X\rangle} = \delta_{\mathbf{K}_{\mathrm{CM}f}-\mathbf{q}_{2\parallel}-\mathbf{K}_{\mathrm{CM}X}} \delta_{\tau_f-\tau_X} \frac{\tilde{\varphi}_{nS}(\mathbf{k}_{hf})}{\sqrt{S}} (\boldsymbol{\Pi}_2)^{|f\rangle}_{|X\rangle}, \tag{3}$$

where $\tilde{\varphi}_{nS}(\mathbf{k}) = \int d\boldsymbol{\rho}\, \varphi_{nS}(\boldsymbol{\rho}) \exp(-i\mathbf{k} \cdot \boldsymbol{\rho})$, and $(\boldsymbol{\Pi}_2)^{|f\rangle}_{|X\rangle} \approx \langle 0, k_{fz}; \tau_f, j_f | \mathbf{p} | c; \tau_X \rangle$ is the interband momentum matrix element evaluated at the edge of the 2D BZ in the dipolar approximation ($\mathbf{q}_2 \to \mathbf{0}$). It turns out that only states near the BZ corners contribute to the tr-ARPES, notably for two

reasons: because of the Fourier mapping $\tilde{\varphi}_{nS}(\mathbf{k}_{hf})$, and because of $q_{n\parallel} \ll$ BZ size (even for the high excitation energy necessary for $\hbar\omega_2$ to surpass the extraction energy $\approx$ typically a few tens eV). Additionally, one explicitly gets in Eq. (3) the momentum conservation $\mathbf{K}_{\mathrm{CM}f} = \mathbf{q}_{2\parallel} + \mathbf{q}_{1\parallel}$ expected from the in-plane translation invariance of the problem. One also gets the valley conservation $\tau_f = \tau_X$, indicative of the fact that the probe is by far unable to flip the carriers' valley from the initial exciton one.

Finally, for given pump and probe characteristics (incidence and polar angles, spectral profiles), the possible final states are characterized by four parameters: the valley τ_f, the free band j_f of this valley, the 2D wave vector $\mathbf{k}_{hf}$ for the final valence hole, and the wave vector $\mathbf{k}_{fz}$ that characterizes the final electron Oz motion. The total photoemission probability should be summed over these four parameters. It is worth stressing that they appear only in the $C_\nu(T_2)$ function and/or in the $\mathbf{\Pi}_2$ matrix element, but not in the pump matrix element Eq. (2); we will come back to this point later. In the following, we discuss some consequences of the previous results on the spin- and time-resolved exciton-mediated ARPES measurements.

III. SYMMETRY AND LOCKING PROPERTIES OF UNBOUND STATES

Let us first consider the current-valley locking for the emitted electrons. To this end, we restrict ourselves to the case of a circularly polarized pump under normal incidence, which can only generate excitons in a given valley, say the $\tau = +1$ one for an $\hat{\boldsymbol{\sigma}}_{(+)}$ excitation (a more general situation is discussed later). Let us also fix k_{fz} and consider only the ground state $1S$-excitons: in this case, the summation over $|\nu\rangle$ in Eq. (1) is restricted to this sole intermediate state. Moreover, $|\mathbf{k}_{f\parallel}| = |\mathbf{k}_{hf} + \mathbf{K}_{\mathrm{CM}f}| \ll K_0$, so that the in-plane projection of the emitted free-electron total momentum is largely determined by its valley component: $\mathbf{p}_{f\parallel} = \hbar\mathbf{K}_{\tau_f, j_f}$. Electrons are thus emitted within relatively narrow cones in the in-plane momentum space, centered at the $\hbar\mathbf{K}_{\tau_f, j_f}$ mean directions; in the remainder of the paper, we call such a pretty directive emission cone (or emission lobe) a "pocket." Since $\mathbf{K}_{(\tau_f, j_f=1,2,3)}$ corresponds to three vectors with the same norm K_0 but rotated by 120° from each other, the outgoing electron current related to a given valley is actually formed by three currents, of the same intensities but with polar directions 120° rotated from each other. Of course, the same analysis holds true for the $\tau = -1$ valley under $\hat{\boldsymbol{\sigma}}_{(-)}$ polarization excitation, which also leads to a three-current pattern that is, however, 60° rotated with respect to the $\tau = +1$ one. Thus, for each of the three currents for a given valley, one obtains after light circular polarization reversal a current with reversed in-plane direction (since $\mathbf{K}_{(-\tau, j)} = -\mathbf{K}_{(+\tau, j)}$). For a linearly polarized pump excitation, the two valley contributions to the escape current combine (see below) to give the six-pocket pattern recently evidenced in tr-ARPES measurements [48,58]. It is worth reinforcing this point: a circularly polarized pump under normal incidence is expected to generate a three-pocket pattern in place of the six-pocket one, indicative of a single-valley contribution. Moreover, reversing the pump circular polarization (while keeping everything else constant) would generate the sole complementary three-pocket pattern related to the opposite valley. Finally, a π-rotation of the sample (at constant excitation and detection parameters, or, equivalently, a π-rotation of the whole experimental setup) interchanges the $+1$ and -1 valleys and would lead to probe the reversed current. Interestingly, these features for the photoejected electron outside the sample also characterize the VHE, which involves currents inside the TMD layer in the presence of an applied bias (absent in our case). tr-ARPES appears to be a technique to externally visualize the momentum-valley locking effect. The analogy with the VHE is further developed below.

For now, let us put the previous discussion on a more quantitative basis, using Eqs. (1), (2), and (3) for the probability amplitude. By considering only $1S$ excitons and neglecting small COM ($\mathbf{K}_{\mathrm{CM}X}$ and $\mathbf{K}_{\mathrm{CM}f}$) and light wave vectors ($\mathbf{q}_n$), one obtains for the integrated (over $\mathbf{k}_{hf}$ and k_{fz}) probability related to the pocket (τ_f, j_f)

$$P_{(\tau_f, j_f)} = \bar{P}_{j_f} |\hat{\boldsymbol{\epsilon}}_1 \cdot \hat{\boldsymbol{\sigma}}^*_{\tau_f}|^2, \tag{4a}$$

$$\bar{P}_{(j_f)} = |\varphi^*_{1S}(0)\Pi_{(\tau_f)}|^2 \sum_{\mathbf{k}_{hf}, k_{fz}} |C_{f,1S}(T_2)\tilde{\varphi}_{1S}(\mathbf{k}_{hf})\, \hat{\boldsymbol{\epsilon}}_2 \cdot \langle 0, k_{fz}; \tau_f, j_f | \mathbf{p} | c; \tau_f \rangle|^2, \tag{4b}$$

where $f = (\mathbf{k}_{hf}, k_{fz}; \tau_f, j_f)$ in $C_{f,1S}(T_2)$. It can be shown that $\bar{P}_{j_f}$ is independent of τ_f, due to the time-reversal symmetry [59] and to the summations over $(\mathbf{k_{hf}}, k_{fz})$. A circularly polarized pump $\hat{\boldsymbol{\epsilon}}_1 = \hat{\boldsymbol{\sigma}}_{(\tau)}$ excites only the pockets $(\tau_f = \tau, j_f)$, and a reversing polarization $\hat{\boldsymbol{\epsilon}}_1 = \hat{\boldsymbol{\sigma}}_{(-\tau)}$ also reverses the pockets profile (more precisely, its in-plane projections). Note that the small $\mathbf{k}$-space extension imposed by $\tilde{\varphi}_{1S}(\mathbf{k}_{hf})$ ($|\Delta\mathbf{k}_{hf}| \ll K_0$) and by the energy-momentum resolution of the analyzer (which may severely limit Δk_{fz}) ensures that there is no pocket overlap, and it allows us to unambiguously define the integrated pocket current [see Eq. (4)].

Let us now further deepen the analysis of the electron currents in a tr-ARPES experiment and consider its spin characteristics. To this end, we recall that the valence and conduction states $|B = v, c; \tau\rangle$ involved in the exciton formation have been shown to be well described by uncoupled $|\text{orbital}\rangle \otimes |\text{spin}\rangle$ states, which are valley-governed and such that both the spin and electron orbital momentum projections along the Oz direction are reversed for the $+1$ and -1 valleys (time-reversal symmetry). Since the dipolar coupling to the probe light is spin-diagonal, the outgoing electron carries the same spin it had in the initial exciton. As a consequence, the exciton-mediated tr-ARPES experiments would generate currents that are ideally 100% spin-polarized and 100% valley-polarized (again since the different "pockets" are well resolved by the analyzer with no overlap because of the

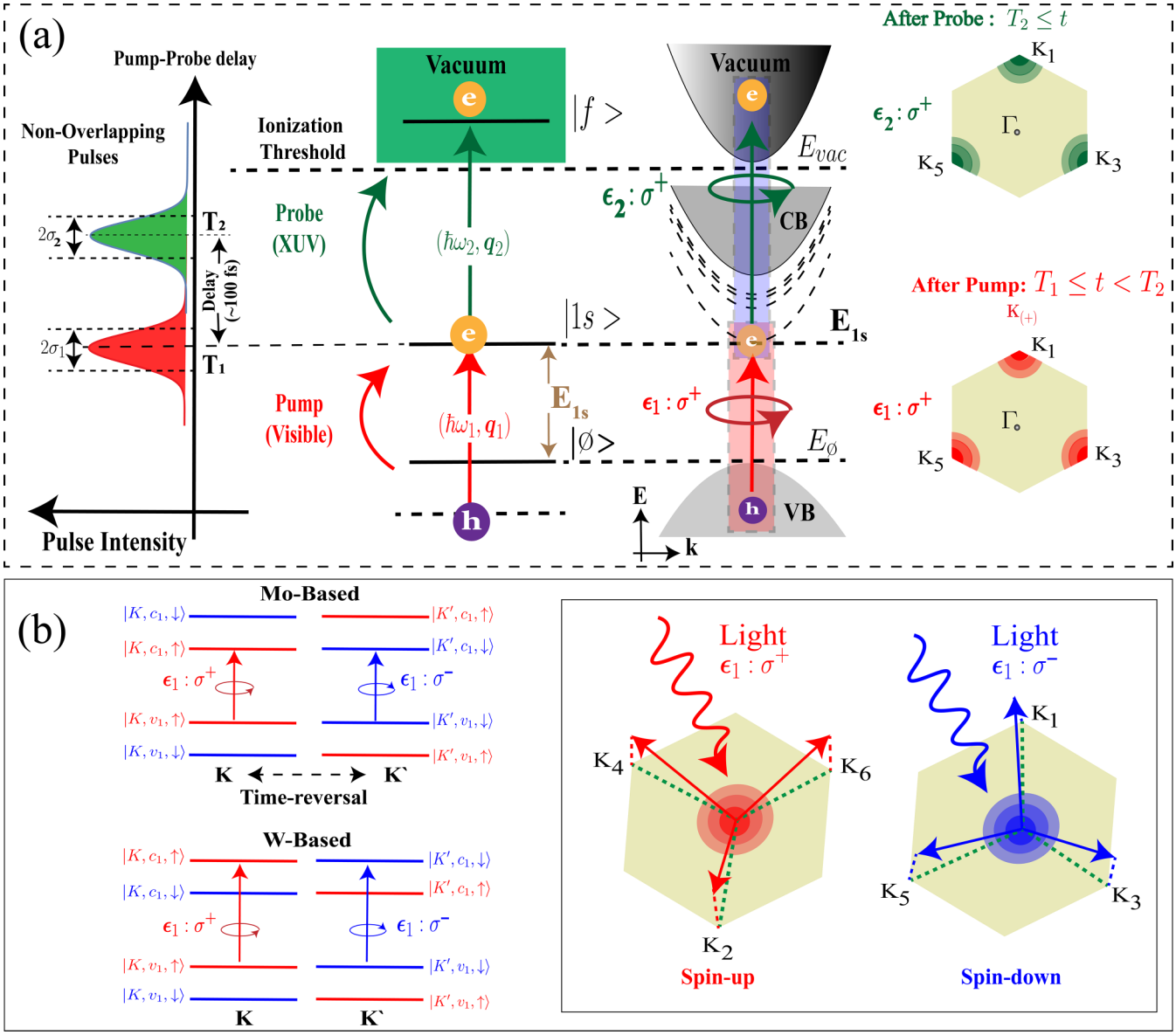

FIG. 2. (a) Schematic representation of the pump and probe sequential excitations for a single electron, showing, in particular, the two nonequivalent (time-reversed) sets of three final bands in the continuum, around the $\mathbf{K}_{(+)}$ and $\mathbf{K}_{(-)}$ edges. For circular pump polarization under normal incidence, the whole process is valley-conserving: the photoejected electron remains near its original edge in the valence band, so that the available final states for the probe are very effectively filtered by the pump. Note that the fully occupied VB is assumed to lie at $E_{\phi} = 0$ eV and the CB minimum is energetically situated at the band gap. The envelope of the pump/probe pulse of temporal width σ_n centered around time T_n with a Gaussian profile. (b) Illustration of the spin-momentum-valley locking effect, for Mo-based and W-based, expected for the ARPES current resulting from a circular pump polarization under normal incidence.

important Fourier mapping of *Wannier-Mott* excitons and small Δk_{fz}). In conclusion, spin-resolved tr-ARPES using a circularly polarized pump under normal incidence excitation would allow direct visualization of the simultaneous momentum, spin, and valley locking. This triple locking is schematically represented in Fig. 2.

It follows from the previous discussions that the photocurrent from tr-ARPES (that results from a two-excitation process) is a valley-discriminant process, to be aligned with interband dichroism and VSL (related to a single interband excitation). It shares various features with the VHE effect, such as (i) the bijective links between any two of the three characteristics: **K**-valley, spin orientation, and triple (120° rotated) current directions, and (ii) the possibility to externally monitor them (reversing the bias in VHE and the pump polarization in tr-ARPES). This common phenomenology is not fortuitous. Indeed, VHE relies on the Berry curvature of the conducting states, which is tightly related to the actual carrier valley (it reverses sign under valley exchange), and analogously, the spin and the propagation directions of photoejected electrons are closely related to the exciton valley. To further clarify the analogy, let us consider the average final current $\langle \mathbf{p} \rangle = \langle \Psi | \mathbf{p} | \Psi \rangle$, with Ψ the time-evolved wave function [the same used to obtain Eq. (1)]. For a given pump polarization,

the vacuum current is proportional to

$$\langle \mathbf{p} \rangle_{\rm vac} \approx \sum_f \hbar \mathbf{K}_f |A_f|^2 = \sum_{\tau_f, j_f} \langle \mathbf{p} \rangle_{{\rm vac}(\tau_f, j_f)}, \tag{5}$$

where $f = (\mathbf{k}_{hf}, k_{fz}; \tau_f, j_f)$. The total current on one side of the TMD layer is thus a sum of six contributions, $\langle \mathbf{p} \rangle_{{\rm vac}(\tau_f, j_f)}$. Its in-plane component vanishes when summed over all possible final states, since $\sum_{j=1,2,3} \mathbf{K}_{(\tau,j)} = 0$. For circular polarization, only three $\langle \mathbf{p} \rangle_{{\rm vac}(\tau_f, j_f)}$ do not vanish and give the three-pockets, as we discussed above. For any j_f there is $\langle \mathbf{p} \rangle_{{\rm vac}(-\tau_f, j_f)} = -\langle \mathbf{p} \rangle_{{\rm vac}(+\tau_f, j_f)}$ since $\mathbf{K}_{(-\tau,j)} \equiv -\mathbf{K}_{(+\tau,j)}$: the in-plane current reverses direction for reversed pump polarization, like the in-plane VHE current (or the lateral bias that it induces) reverses direction (sign) under bias reversal.

IV. INTERVALLEY EXCHANGE EFFECTS

For oblique pump incidence, the photoexcited excitons have a nonvanishing COM wave vector. Excitons with the same $\mathbf{K}_{\rm CMX}$ but pertaining to different valleys are coupled by the exchange part of the Coulombic interaction [34,35]. Let us then consider its role in the photoemission process (we restrict the discussion to a single $\nu = 1S$ state, which excludes $1S - 2S$ intravalley beatings [60]). The exchange coupling is due to the long-range part of the Coulomb potential, which is able to admix states of different valleys. The intervalley excitonic mixing has been discussed in a few papers [25,34,45,61]. Following these works, the coupling of the two $1S$ states $|1S, \mathbf{K}_{\rm CMX}; \tau_X = \pm 1\rangle$ (or $|\pm X\rangle$ in short), with the same in-plane wave vector $\mathbf{K}_{\rm CMX}$ and energy $E_{1S}(\mathbf{K}_{\rm CMX})$ but attached to different valleys, generates the valley-mixed states $|1S, \mathbf{K}_{\rm CMX}; \eta = \pm 1\rangle$ (or in short $|\eta\rangle$):

$$|\eta\rangle = \frac{1}{\sqrt{2}} (e^{-i\theta_{\rm CMX}} |+X\rangle - \eta\, e^{+i\theta_{\rm CMX}} |-X\rangle), \tag{6a}$$

$$E_\eta = E_{1S}(\mathbf{K}_{\rm CMX}) + \eta\, \hbar \Omega_{1S}^{\rm exc}(\mathbf{K}_{\rm CMX}). \tag{6b}$$

They are the symmetrical and antisymmetrical combinations of the two independent excitons $|\pm {\rm X}\rangle$. $\theta_{\rm CMX}$ is the in-plane direction of $\mathbf{K}_{\rm CMX}$, and $\hbar\Omega_{1S}^{\rm exc}(\mathbf{K}_{\rm CMX})$ is the intervalley exchange coupling (roughly proportional to $\mathbf{K}_{\rm CMX}$ for small COM wave vectors, as calculated, e.g., in [34]). Finally, $E_{1S}(\mathbf{K}_{\rm CMX}) = E_{1S}(0) + \hbar^2 \mathbf{K}_{\rm CMX}^2 / 2M_{\rm CMX} \approx E_{1S}(0)$, with $M_{\rm CMX}$ the sum of the electron and hole effective masses. One has then

$$A_f \approx C_{1S}(T_2) \sum_\eta \hat{\boldsymbol{\epsilon}}_2 \cdot (\boldsymbol{\Pi}_2)_\eta^f e^{-i\eta \Omega_{1S}^{\rm exc} T_2}\, \hat{\boldsymbol{\epsilon}}_1 \cdot (\boldsymbol{\Pi}_1)_\emptyset^\eta, \tag{7}$$

where the weak dependence of $I(T_2)$ on the small exchange energy $\hbar\Omega_{1S}^{\rm exc}$ was neglected: $I_{\omega_f, \omega_{v\eta}}(T_2) \approx I_{\omega_f, \omega_v}(T_2)$ so that $C_{1S}(T_2)$ is the same as in Eq. (1b). Considering that the final electron and hole states both sit near τ_f (recall that we neglect any Coulombic coupling in the final states), only $|\tau_f X\rangle$ contributes to the probe-related $\boldsymbol{\Pi}_2$ matrix elements, and one gets

$$A_{\tau_f} \approx C_{1S}(T_2) \tau_f \frac{e^{-i\tau_f \theta_{\rm CMX}}}{\sqrt{2}}\, \hat{\boldsymbol{\epsilon}}_2 \cdot (\boldsymbol{\Pi}_2)_{|\tau_f X\rangle}^{|f\rangle} \times \sum_\eta e^{-i\eta \Omega_{1S}^{\rm exc} T_2}\, \hat{\boldsymbol{\epsilon}}_1 \cdot (\boldsymbol{\Pi}_1)_{|\emptyset\rangle}^{|\eta\rangle}. \tag{8}$$

The matrix element of $\boldsymbol{\Pi}_2$ is the same as in Eq. (3) (for $\tau_X = \tau_f$). The pump contribution is the same as in Eq. (2) after the replacement

$$\hat{\sigma}^*_{(\tau_X)} \Pi_{(\tau_X)} \to \frac{1}{\sqrt{2}} (e^{+i\theta_{\rm CMX}} \hat{\sigma}^*_{(+)} \Pi_{(+)} - \eta\, e^{-i\theta_{\rm CMX}} \hat{\sigma}^*_{(-)} \Pi_{(-)}). \tag{9}$$

One has then

$$A_{\tau_f} \approx C_{1S}(T_2)\, \tau_f \hat{\boldsymbol{\epsilon}}_2 \cdot (\boldsymbol{\Pi}_2)_{|+X\rangle}^{|f\rangle} \delta_{\mathbf{K}_{\rm CMX} - \mathbf{q}_{1\parallel}} \times \sqrt{S}\, \varphi^*_{nS}(0) \Pi_0\, e^{-i\tau_f \theta_{\rm CMX}} A^{\rm pump}_{\tau_f = \pm 1}, \tag{10a}$$

$$A^{\rm pump}_{\tau_f} = \hat{\boldsymbol{\epsilon}}_1 \cdot \big(\cos\big(\Theta_{1S}^{\rm exc}\big) e^{i\theta_{\rm CMX}} \hat{\sigma}^*_{(\tau_f)} \pi_{(\tau_f)} + i \sin\big(\Theta_{1S}^{\rm exc}\big) e^{-i\,\theta_{\rm CMX}} \hat{\sigma}^*_{(-\tau_f)} \pi_{(-\tau_f)} \big), \tag{10b}$$

where we define the phase $\Theta_{1S}^{\rm exc} = \Omega_{1S}^{\rm exc}\, T_2$, and $\pi_{(\tau)} = \Pi_{(\tau)}/\Pi_0$ are normalized matrix elements that verify $\pi_{(-)} = -(\pi_{(+)})^*$, and $\Pi_0 = |\Pi_{(\pm)}|$. One easily recovers the previous results for the case of normal pump excitation [i.e., for $\Omega_{1S}^{\rm exc}(0) = 0$]. One already sees that the exchange coupling brings two effects: it modifies [by a $\cos(\Theta_{1S}^{\rm exc})$ factor] the intravalley probability, and, most importantly, it allows a valley-flip process [term with $\sin(\Theta_{1S}^{\rm exc})$ factor] for propagating excitons. These effects will be considered at length below. $A^{\rm pump}_{\tau_f}$ carries all information related to the pump excitation [aside from its spectral profile, included in the $C_{1S}(T_2)$ function]. It does not depend on the final wave vectors $\mathbf{k}_{hf}$ and k_{zf}, and thus its absolute square appears as a multiplicative factor when the summation over these wave vectors is performed to obtain the integrated photoemission probability (or the integrated photocurrent) for a pocket. This parameter allows us to focus on the control of the electron photoejection process related to the sole pump excitation. We define correspondingly the normalized integrated signal $P^{\rm pump}_{\tau_f} = |A^{\rm pump}_{\tau_f}|^2$ for any of the three pockets of the τ_f valley.

Role of pump excitation configuration

For an oblique pump with incidence and polar angles $\theta_{\rm inc}$ and $\phi_{\rm inc}$, respectively, and arbitrary electric field polarization (E_X, E_Y) fulfilling $|E_X|^2 + |E_Y|^2 = 1$ and lying in the plane (X, Y) orthogonal to the wave vector $\mathbf{q}_1$ (along the OZ axis), one has

$$\hat{\boldsymbol{\epsilon}}_1 \cdot \hat{\boldsymbol{\sigma}}^*_{(\pm)} = \frac{1}{\sqrt{2}} (E_X \cos(\theta_{\rm inc}) \mp i E_Y) e^{\mp i\phi_{\rm inc}}, \tag{11a}$$

$$\hat{\boldsymbol{\epsilon}}_1 \cdot \hat{\boldsymbol{\sigma}}^*_{(\tau)} = \frac{1}{\sqrt{2}} (E_X \cos(\theta_{\rm inc}) - i\tau E_Y) e^{-i\tau\phi_{\rm inc}}. \tag{11b}$$

For completeness, we give also the Oz component $\hat{\boldsymbol{\epsilon}}_1 \cdot \hat{\mathbf{z}} = E_X \sin(\theta_{\rm inc})$. Note that $\hat{\boldsymbol{\sigma}}_{(\pm)}$ are defined with respect to the crystalline axis in the TMD (x, y) plane, and the polar angle $\phi_{\rm inc}$ is the angle between the projection of the OX axis in the (x, y) plane and the Ox axis in this plane (see Fig. 3). For normal incidence $\phi_{\rm inc}$ becomes undetermined. The $\delta_{\mathbf{K}_{\rm CMX} - \mathbf{q}_{1\parallel}}$ in Eq. (2) imposes that $\theta_{\rm CMX} = \phi_{\rm inc}$, so that the final photoejection probability is independent of the pump polar angle, for any polarization $\hat{\boldsymbol{\epsilon}}_1$. Finally, $P^{\rm pump}_{\tau_f}$ depends on four parameters: field polarization (E_X, E_Y), incident angle $\theta_{\rm inc}$, and pump-probe delay T_2 [as mentioned, the pump spectral profile, more difficult to modify in the experiments, appears only in

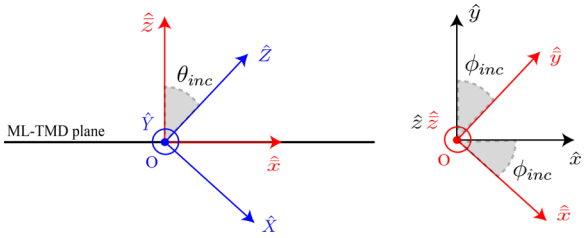

FIG. 3. Schematic illustrating of the polar $\phi_{\rm inc}$ and incidence angles $\theta_{\rm inc}$, as referenced to the crystalline axis. We note $(OXYZ)$ is the referential for the incoming light, $\mathbf{q} = q\hat{\mathbf{Z}}$, and polarization $\mathbf{E} = E_X\hat{\mathbf{X}} + E_Y\hat{\mathbf{Y}}$. $(O\bar{x}\bar{y}\bar{z})$ is the referential for projection of $(OXYZ)$ in the TMD plane, by a rotation of $(OXYZ)$ around the $O\bar{y} \equiv OY$ axis. $O\bar{z}$ is perpendicular to the TMD plane. $(Oxyz)$ is the crystal (real-space) axis, which can be different from $(O\bar{x}\bar{y}\bar{z})$ by a rotation around $Oz \equiv O\bar{z}$ axis.

the function $I(T_2)$]. Using the expression of $\hat{\boldsymbol{\epsilon}}_1 \cdot \hat{\boldsymbol{\sigma}}^*_{(\tau)}$ enables us to write [62]

$$P^{\rm pump}_{\tau_f} = C_I I + C_Q Q + C_V V + C_U U, \tag{12a}$$

$$C_I \equiv C_I(\theta_{\rm inc}) = \frac{1+\cos^2(\theta_{\rm inc})}{4}, \tag{12b}$$

$$C_Q \equiv C_Q(\theta_{\rm inc}) = -\frac{\sin^2(\theta_{\rm inc})}{4}, \tag{12c}$$

$$C_V \equiv C_V\left(\theta_{\rm inc}; \Theta^{\rm exc}_{1S}; \tau_f\right) = \tau_f \frac{\cos(\theta_{\rm inc})}{2}\cos\left(2\Theta^{\rm exc}_{1S}\right), \tag{12d}$$

$$C_U \equiv C_U\left(\theta_{\rm inc}; \Theta^{\rm exc}_{1S}; \tau_f\right) = \tau_f \frac{\cos(\theta_{\rm inc})}{2}\sin\left(2\Theta^{\rm exc}_{1S}\right) \tag{12e}$$

in terms of the four Stokes parameters $I = |E^2_X| + |E^2_Y| = 1$, $Q = |E^2_X| - |E^2_Y|$, $U = 2\,\mathrm{Re}\{E_X E^*_Y\}$, and $V = -2\,\mathrm{Im}\{E_X E^*_Y\}$ that completely define the polarization state of the pump field. As expected, the total integrated probability per pocket $P^{\rm pump}_{+1} + P^{\rm pump}_{-1} = 1 - |\hat{\boldsymbol{\epsilon}}_1 \cdot \hat{\mathbf{z}}|^2$ decreases with increasing incidence angle. We note the central roles of the valley-dependent parameters C_U and C_V, and thus also of the U and V Stokes parameters, which considerably change with the pump polarization. In the following, we consider some configurations of interest, as usually implemented in polarization experiments.

Circular polarization. For $\hat{\boldsymbol{\epsilon}}_1$ corresponding to a $\hat{\boldsymbol{\sigma}}_{(\pm)}$ circular excitation, which we denote hereafter $\Sigma_{(\pm)}$, $E_Y/E_X = \pm i$, and one gets $\hat{\boldsymbol{\epsilon}}_1 \cdot \hat{\boldsymbol{\sigma}}_{(\tau)} \to \frac{1}{2}[\cos(\theta_{\rm inc}) \pm \tau]e^{-i\tau\phi_{\rm inc}}$, $Q = U = 0$, $V = \pm 1$, and thus

$$P^{{\rm pump}\ \Sigma_{(\pm)}}_{\tau_f} = \frac{1}{4}[\cos(\Delta\theta_{\rm inc}) \pm \tau_f\tau_N]^2 \mp \tau_N \cos(\Delta\theta_{\rm inc})\sin^2\left(\Theta^{\rm exc}_{1S}\right), \tag{13}$$

where $\theta_{\rm inc} \to \theta_N = 0$ or π are the two normal incidence angles, and we defined $\Delta\theta_{\rm inc} = \theta_{\rm inc} - \theta_N$ as the deviation with respect to the perpendicular incidence, and $\tau_N = \cos(\theta_N)$. For the particular case of normal incidence, i.e., for $\Delta\theta_{\rm inc} = 0$, the second term in Eq. (13) vanishes since $\Omega^{\rm exc}_{1S} \propto \sin(\Delta\theta_{\rm inc})$. It results from the first term that opposite valleys can be excited with the same probability by pumps of the same polarization but impinging normally on the suspended TMD layer from opposite sides (from above or below): Indeed, for a fixed pump polarization, an observer looking e.g., at the counter-propagating direction sees opposite electric field rotations at the position $z = 0$ of the layer in each case.

Let us consider now an excitation under oblique incidence at $\theta_N = 0$. The first term in Eq. (13) gives, respectively, $[\cos(\theta_{\rm inc}/2)]^4$ and $[\sin(\theta_{\rm inc}/2)]^4$ for $\Sigma_{(\tau_f)}$ and $\Sigma_{(-\tau_f)}$ pumps, which simply reflects the fact that a circularly polarized light under non-normal incidence has both $\hat{\boldsymbol{\sigma}}_{(\pm)}$ in-plane components (a "geometrical" or "projection" factor). The second term is due to the intervalley exchange coupling. It vanishes at normal incidence, while for an oblique excitation it oscillates with the pump-probe delay with a period $\Delta T_2 = \pi/\Omega^{\rm exc}_{1S}$ that decreases fast with increasing $\theta_{\rm inc}$. It is worth stressing again that the second term corresponds to an exciton valley-flip process. To further clarify this point, let us consider first the $\Sigma_{(-\tau_f)}$ contribution to the τ_f valley signal for small $\theta_{\rm inc}$, as given by $P^{{\rm pump}\ \Sigma_{(-\tau_f)}}_{\tau f}$. The first term $[\sin(\theta_{\rm inc}/2)]^4$ represents a cross-generation process, namely, it comes from the fact that a $\Sigma_{(-\tau_f)}$ pulse has a small probability to generate an exciton directly at $\mathbf{K}_{(\tau_f)}$, from where the probe photoexcitation occurs. However, a $\Sigma_{(-\tau_f)}$ pulse also generates (with much higher probability) an exciton at $K(-\tau_f)$, which suffers an exchange-assisted valley-flip towards the $K(\tau_f)$ valley, from where the probe photoexcitation occurs. It is now important to note that for a $\Sigma(-\tau_f)$ pump under small incidence angles, the activation of the escape channel with increasing $\theta_{\rm inc}$ is largely dominated by the valley-flip process, which gives a $\theta^2_{\rm inc}$ variation, much faster than the $\theta^4_{\rm inc}$ one from the geometrical term. A similar reasoning applied to a $\Sigma(\tau_f)$ pulse ($P^{{\rm pump}\ \Sigma_{(\tau_f)}}_{\tau_f}$ term) enables us to understand that the exchange process decreases its photogeneration rate, as compared to the rate in the absence of exchange coupling, in stark contrast with the previous increasing rate for a $\Sigma(-\tau_f)$ pulse [see the sign of the second term in Eq. (13)]. In conclusion, we state that (i) the tr-ARPES signal should evolve from a three-pocket profile at normal incidence, to six pockets, with opposite-valley contribution increasing with increasing $\theta_{\rm inc}$; (ii) the activation of the time-reversed currents is related not only to the geometrical factor but also, and principally, to the intervalley exchange coupling for propagative exciton, and (iii) for a given current direction (orientation of the analyzer in one pocket region) the value of the current can be continuously varied by changing the pump incidence angle, without losing the triple momentum-spin-valley locking.

Quarter-wave ($\lambda/4$) polarization. Let us briefly consider the more general pump polarization generated by a quarter-wave plate. For an initially TM polarized pump (as is often the case in experiments), the rotated field becomes $(E_X, E_Y) = (1 - i\cos(2\Theta_{\rm QW}), -i\sin(2\Theta_{\rm QW}))/\sqrt{2}$, where $\Theta_{\rm QW}$ is the rotation angle of the plate. For $\Theta_{\rm QW} = \mp\pi/4$, one recovers the $\Sigma(\pm)$ case. We obtain

$$P^{{\rm pump}\ (\lambda/4)}_{\tau_f} = A + \left(C_Q/2\right)\cos(4\Theta_{\rm QW}) + (C_U/2)\sin(4\Theta_{\rm QW}) - C_V\sin(2\Theta_{\rm QW}), \tag{14}$$

where $A = C_I + C_Q/2$. This expression may prove to be convenient to check experimentally since the whole setup remains fixed except for the angle $\Theta_{\rm QW}$ of the polarizer.

Half-wave ($\lambda/2$) *linear polarization*. A half-wave polarizer transforms an initially TM polarized pump into the field $(E_X, E_Y) = -i(\cos(2\Theta_{\rm HW}), \sin(2\Theta_{\rm HW}))$, where $\Theta_{\rm HW}$ is the $\lambda/2$ rotation angle; in particular, $2\Theta_{\rm HW} = 0[\pi]$ and $2\Theta_{\rm HW} = \pi/2[\pi]$ for the TM and TE linear polarizations, respectively. One gets $V = 0$ and then

$$P_{\tau_f}^{\text{pump }(\lambda/2)} = C_I(\theta_{\rm inc}) + C_Q \cos(4\Theta_{\rm HW}) + C_U \sin(4\Theta_{\rm HW}). \tag{15}$$

For perpendicular incidence, the integrated probability is of course polarization- and valley-independent. Note that the $\mathbf{K}_{(+)}$ and $\mathbf{K}_{(-)}$ valleys possess the same excitonic spectrum, which can be simultaneously excited by a linearly polarized pump, even at normal incidence. That seems to play against the observation of the current-spin-valley locking, since the linear pump generates a coherent superposition of the $\mathbf{K}_{(+)}$ and $\mathbf{K}_{(-)}$ degenerated excitons. However, contributions of excitons from different valleys do not interfere in A_f, since they can never lead to the same final state for the emitted electron [as discussed above, notably because of the pockets exclusion (absence of pockets overlap)]. The sole effect of using a linear instead of a circular pump polarization is thus to allow simultaneous observation of the full six-pockets pattern (as reported in the experiments [58]).

Under oblique incidence, one obtains a difference between TE and TM modes, but both are independent of the valley-dependent term $C_U(\theta_{\rm inc}; \Theta_{1S}^{\rm exc}; \tau_f)$. This coefficient may nevertheless be obtained from the measurement of $P^{\text{pump }(\lambda/2)}$ as a function of the $\lambda/2$ plate orientation $\Theta_{\rm HW}$ at non-normal incidence.

In conclusion, a continuous variation of pump polarization (as, e.g., modulated by a $\lambda/2$ or $\lambda/4$ plate) would lead to a continuous evolution of the tr-ARPES pattern and escape probability, which would in turn enable us to extract (via, e.g., a fitting procedure) valuable information about the valley-flip exchange coupling.

V. DISCUSSIONS AND CONCLUSION

Scatterings may prove detrimental to the observation of the effects discussed above by introducing bright-to-dark population exchanges and damping any initial coherent superposition of the $\mathbf{K}_{(\pm)}$ exciton states. We shall not consider in detail scattering processes, which are well beyond the scope of this work, but only address a few qualitative considerations in relation to the exciton-mediated ARPES experiments. The pump excitation generates excitons inside the light cones around the $\mathbf{K}_{(+)}$ and/or $\mathbf{K}_{(-)}$ transitions, and thus $0 \leqslant K_{\rm CMX} \leqslant K_{\rm CMX(MAX)}$. At the cone edge ($K_{\rm CMX} = K_{\rm CMX(MAX)}$), one has that $\hbar\Omega_{1s}^{\rm exc}$ is roughly in the meV range [34,54,63], corresponding to a characteristic coherent valley-flip time $T_{vf} = \pi/\Omega_{1s}^{\rm exc}$ in the ps timescale for the $1S$ excitons. This is much smaller than radiative lifetime $\tau_{\rm rad}$ at moderate and high temperatures [37]. To discuss the role of scatterings, it is convenient to distinguish between intravalley and intervalley processes. Let us start with the first case, and consider first elastic processes characterized by a momentum scattering time $\tau_{\rm sc}$. Under the favorable condition $T_{vf}, T_2 < \tau_{\rm sc}, \tau_{\rm rad}$ (as is possibly the case for clean molybdenum-based samples at low or moderate temperatures), the pulse at delay T_2 is able to extract the electron from the exciton before scattering occurs, allowing us to probe the coherent valley-flip process under the action of the intervalley coupling. In the opposite limit of frequent intravalley scatterings such that $\tau_{\rm sc}\Omega_{1s}^{\rm exc} \ll 1$, the valley-flip becomes highly inhibited, with a rate $\tau_{\rm sc}(\Omega_{1s}^{\rm exc})^2/2$ (motional narrowing regime or D'yakonov-Perel' mechanism [38,39]). Inelastic (phonon-assisted) intravalley processes may also play an important role. Since the typical phonon energy is much smaller than the $1S-2S$ detuning, such scatterings generate incoherent $1S$ excitons with much bigger $K_{\rm CMX}$ (i.e., well beyond the light cone), for which the intervalley coherent coupling is also much bigger. If the spectral resolution of the experiments is lower than the energy distribution of the phonon-broadened population (of the order of the phonon energy), both exciton populations inside and outside the light cone contribute to the measured ARPES signal from a given valley. Scatterings in this case are thus expected to sizeably increase the intervalley exchange effect on the photocurrent signal.

Phonon-assisted intervalley scatterings may efficiently redistribute the pump-generated exciton population among the various $\mathbf{K}$ and $\mathbf{Q}$ valleys, in a time τ_{iv} of a few hundred fs [32,48,64,65]. Such processes generate intervalley (or valley-dark) excitons by transferring the electron towards either the $\mathbf{K}_{(-\tau)}$ or some of the $\mathbf{Q}$ valleys [48,65,66]. We quote two main consequences for the ARPES signal: they decrease the initial exciton population by a factor of the order of $\exp(-T_2/\tau_{iv})$, and they trigger the appearance of pockets from other valleys (the opposite $\mathbf{K}$ valley and/or the $\mathbf{Q}$ valleys). $\mathbf{Q}$-related pockets were actually experimentally observed [48]. The $\mathbf{K}_{(+)} \leftrightarrow \mathbf{K}_{(-)}$ population exchange decreases the pump-induced intensity contrast of time-reversed pockets, as well as breaking to some extent the triple-locking effect discussed above. In fact, phonon scatterings are essentially spin-conserving processes. For instance, $\mathbf{K}_{(+)} \rightarrow \mathbf{K}_{(-)}$ events transfer spin-up electrons into the $\mathbf{K}_{(-)}$ valley, from where they are extracted, thus contributing to a decrease of the spin-polarization of this valley. Note that the energy of the extracted electrons differs by roughly one phonon energy from the "native" $\mathbf{K}_{(-)}$ ones (assuming the same binding energy for the bright and valley-dark excitons), and they could in principle be distinguished from each other. However, the ARPES experiments reported so far were not able to resolve between the two exciton species, suggesting that the energy shift accompanying the phonon-related valley-flip of the electron is sizeably smaller than intrinsic and/or inhomogeneous pocket broadenings. Note that tungsten-based materials are more subject to the phonon-mediated intervalley redistribution than Mo-based ones, as shown in [67]. However, in both materials, any intervalley transfer should lead to the concomitant appearance of "opposite" $\mathbf{K}$ pockets and/or of $\mathbf{Q}$-related ones, in the same timescale, providing a direct (external) assessment of the internal dynamics of the intervalley processes.

In conclusion, we have considered a detailed theoretical description of the high-energy states that form the escape continuum for photoejected electrons in a tr-ARPES experiment, paying particular attention to their momentum dispersions, time-reversal symmetries, and spin characteristics. The analysis of the various symmetries fulfilled by such unbound states reveals the existence of a momentum-valley locking for the unbound final electron states, sharing various features with the

VHE. Moreover, the photoextracted current ideally presents a robust triple locking of momentum direction, valley origin, and spin orientation, which permits envisioning an on-demand source of highly spin-polarized electrons on vacuum. We have also presented a first study of the robustness of such findings against intervalley processes that tend to suppress (or at best to decrease) the valley-spin polarization of the intermediate exciton states. To this end, we considered in detail the role of Coulomb-exchange driven intervalley coupling. That has allowed us to quantify the dependence of the tr-ARPES measurements upon various setup parameters, such as the incidence angle and light helicity. Finally, we have presented a critical discussion about the role of a few intervalley couplings and/or scattering processes. tr-ARPES appears to be a powerful technique to access the fast dynamic of intervalley couplings and population exchanges. This is largely due to the fact that excitons in ML-TMD have a large binding energy, allowing them to be resonantly excited by a short-pulse pump without putting also into play a large set of dissociated *e-h* pairs, while at the same time remaining relatively localized in momentum space (as compared to typical intervalley distances in the BZ) so that the outgoing pocket currents related to different local valleys can be safely distinguished in the energy-momentum resolved tr-ARPES signal. Our model contains different approximations, such as the use of plane waves for the outgoing electrons, or the neglect of any single-particle spin-mixings affecting the initial exciton state and of any spin-orbit coupling in the final electron state, which may degrade to some extent the final current polarization purity. We hope that our work will stimulate experiments and further theoretical implementations.

ACKNOWLEDGMENTS

The authors acknowledge funding from European Union's Horizon 2020 research and innovation program under Grant Agreement No. 964735 (FET-OPEN EXTREME-IR).

The authors declare no competing interests.

[1] S. Manzeli, D. Ovchinnikov, D. Pasquier, O. V. Yazyev, and A. Kis, 2D transition metal dichalcogenides, Nat. Rev. Mater. **2**, 17033 (2017).

[2] P. Tonndorf, R. Schmidt, P. Böttger, X. Zhang, J. Börner, A. Liebig, M. Albrecht, C. Kloc, O. Gordan, D. R. Zahn *et al.*, Photoluminescence emission and Raman response of monolayer MoS_2, $MoSe_2$, and WSe_2, Opt. Express **21**, 4908 (2013).

[3] K. F. Mak, C. Lee, J. Hone, J. Shan, and T. F. Heinz, Atomically thin MoS_2: A new direct-gap semiconductor, Phys. Rev. Lett. **105**, 136805 (2010).

[4] G.-B. Liu, D. Xiao, Y. Yao, X. Xu, and W. Yao, Electronic structures and theoretical modelling of two-dimensional group-vib transition metal dichalcogenides, Chem. Soc. Rev. **44**, 2643 (2015).

[5] X. Xu, W. Yao, D. Xiao, and T. F. Heinz, Spin and pseudospins in layered transition metal dichalcogenides, Nat. Phys. **10**, 343 (2014).

[6] D. Xiao, G.-B. Liu, W. Feng, X. Xu, and W. Yao, Coupled spin and valley physics in monolayers of MoS_2 and other group-VI dichalcogenides, Phys. Rev. Lett. **108**, 196802 (2012).

[7] W. Feng, Y. Yao, W. Zhu, J. Zhou, W. Yao, and D. Xiao, Intrinsic spin Hall effect in monolayers of group-VI dichalcogenides: A first-principles study, Phys. Rev. B **86**, 165108 (2012).

[8] K. F. Mak, K. L. McGill, J. Park, and P. L. McEuen, The valley Hall effect in MoS_2 transistors, Science **344**, 1489 (2014).

[9] A. Kormányos, V. Zólyomi, N. D. Drummond, P. Rakyta, G. Burkard, and V. I. Fal'ko, Monolayer MoS_2: Trigonal warping, the Γ valley, and spin-orbit coupling effects, Phys. Rev. B **88**, 045416 (2013).

[10] M. M. Glazov, E. L. Ivchenko, G. Wang, T. Amand, X. Marie, B. Urbaszek, and B. Liu, Spin and valley dynamics of excitons in transition metal dichalcogenide monolayers, Physica Status Solidi B **252**, 2349 (2015).

[11] K. F. Mak, K. He, J. Shan, and T. F. Heinz, Control of valley polarization in monolayer MoS_2 by optical helicity, Nat. Nanotechnol. **7**, 494 (2012).

[12] R. Bertoni, C. W. Nicholson, L. Waldecker, H. Hübener, C. Monney, U. De Giovannini, M. Puppin, M. Hoesch, E. Springate, R. T. Chapman, C. Cacho, M. Wolf, A. Rubio, and R. Ernstorfer, Generation and evolution of spin-, valley-, and layer-polarized excited carriers in inversion-symmetric WSe_2, Phys. Rev. Lett. **117**, 277201 (2016).

[13] S. Dong, M. Puppin, T. Pincelli, S. Beaulieu, D. Christiansen, H. Hübener, C. W. Nicholson, R. P. Xian, M. Dendzik, Y. Deng *et al.*, Direct measurement of key exciton properties: Energy dynamics, and spatial distribution of the wave function, Nat. Sci. **1**, e10010 (2021).

[14] M. Puppin, C. W. Nicholson, C. Monney, Y. Deng, R. P. Xian, J. Feldl, S. Dong, A. Dominguez, H. Hübener, A. Rubio, M. Wolf, L. Rettig, and R. Ernstorfer, Excited-state band structure mapping, Phys. Rev. B **105**, 075417 (2022).

[15] F. Wu, F. Qu, and A. H. MacDonald, Exciton band structure of monolayer MoS_2, Phys. Rev. B **91**, 075310 (2015).

[16] G. Wang, A. Chernikov, M. M. Glazov, T. F. Heinz, X. Marie, T. Amand, and B. Urbaszek, *Colloquium*: Excitons in atomically thin transition metal dichalcogenides, Rev. Mod. Phys. **90**, 021001 (2018).

[17] A. Chernikov, T. C. Berkelbach, H. M. Hill, A. Rigosi, Y. Li, O. B. Aslan, D. R. Reichman, M. S. Hybertsen, and T. F. Heinz, Exciton binding energy and nonhydrogenic Rydberg series in monolayer WS_2, Phys. Rev. Lett. **113**, 076802 (2014).

[18] H.-P. Komsa and A. V. Krasheninnikov, Effects of confinement and environment on the electronic structure and exciton binding energy of MoS_2 from first principles, Phys. Rev. B **86**, 241201(R) (2012).

[19] D. Y. Qiu, F. H. da Jornada, and S. G. Louie, Optical spectrum of MoS_2: Many-body effects and diversity of exciton states, Phys. Rev. Lett. **111**, 216805 (2013).

[20] M. M. Ugeda, A. J. Bradley, S.-F. Shi, F. H. Da Jornada, Y. Zhang, D. Y. Qiu, W. Ruan, S.-K. Mo, Z. Hussain, Z.-X. Shen *et al.*, Giant bandgap renormalization and excitonic effects in a monolayer transition metal dichalcogenide semiconductor, Nat. Mater. **13**, 1091 (2014).

[21] Z. Ye, T. Cao, K. O'brien, H. Zhu, X. Yin, Y. Wang, S. G. Louie, and X. Zhang, Probing excitonic dark states in single-layer tungsten disulphide, Nature (London) **513**, 214 (2014).

[22] M. Selig, G. Berghäuser, A. Raja, P. Nagler, C. Schüller, T. F. Heinz, T. Korn, A. Chernikov, E. Malic, and A. Knorr, Excitonic linewidth and coherence lifetime in monolayer transition metal dichalcogenides, Nat. Commun. **7**, 13279 (2016).

[23] M. Selig, G. Berghäuser, M. Richter, R. Bratschitsch, A. Knorr, and E. Malic, Dark and bright exciton formation, thermalization, and photoluminescence in monolayer transition metal dichalcogenides, 2D Mater. **5**, 035017 (2018).

[24] T. Cao, G. Wang, W. Han, H. Ye, C. Zhu, J. Shi, Q. Niu, P. Tan, E. Wang, B. Liu *et al.*, Valley-selective circular dichroism of monolayer molybdenum disulphide, Nat. Commun. **3**, 887 (2012).

[25] T. Yu and M. W. Wu, Valley depolarization due to intervalley and intravalley electron-hole exchange interactions in monolayer MoS_2, Phys. Rev. B **89**, 205303 (2014).

[26] Q. Wang, S. Ge, X. Li, J. Qiu, Y. Ji, J. Feng, and D. Sun, Valley carrier dynamics in monolayer molybdenum disulfide from helicity-resolved ultrafast pump–probe spectroscopy, ACS Nano **7**, 11087 (2013).

[27] C. Mai, A. Barrette, Y. Yu, Y. G. Semenov, K. W. Kim, L. Cao, and K. Gundogdu, Many-body effects in valleytronics: Direct measurement of valley lifetimes in single-layer MoS_2, Nano Lett. **14**, 202 (2014).

[28] L. T. Lloyd, R. E. Wood, F. Mujid, S. Sohoni, K. L. Ji, P.-C. Ting, J. S. Higgins, J. Park, and G. S. Engel, Sub-10 fs intervalley exciton coupling in monolayer MoS_2 revealed by helicity-resolved two-dimensional electronic spectroscopy, ACS Nano **15**, 10253 (2021).

[29] G. Berghäuser, I. Bernal-Villamil, R. Schmidt, R. Schneider, I. Niehues, P. Erhart, S. Michaelis de Vasconcellos, R. Bratschitsch, A. Knorr, and E. Malic, Inverted valley polarization in optically excited transition metal dichalcogenides, Nat. Commun. **9**, 971 (2018).

[30] J. Fu, A. Bezerra, and F. Qu, Valley dynamics of intravalley and intervalley multiexcitonic states in monolayer WS_2, Phys. Rev. B **97**, 115425 (2018).

[31] F. Mujeeb, P. Chakrabarti, V. Mahamiya, A. Shukla, and S. Dhar, Influence of defects on the valley polarization properties of monolayer MoS_2 grown by chemical vapor deposition, Phys. Rev. B **107**, 115429 (2023).

[32] B. R. Carvalho, Y. Wang, S. Mignuzzi, D. Roy, M. Terrones, C. Fantini, V. H. Crespi, L. M. Malard, and M. A. Pimenta, Intervalley scattering by acoustic phonons in two-dimensional MoS_2 revealed by double-resonance Raman spectroscopy, Nat. Commun. **8**, 14670 (2017).

[33] M. Selig, F. Katsch, R. Schmidt, S. Michaelis de Vasconcellos, R. Bratschitsch, E. Malic, and A. Knorr, Ultrafast dynamics in monolayer transition metal dichalcogenides: Interplay of dark excitons, phonons, and intervalley exchange, Phys. Rev. Res. **1**, 022007(R) (2019).

[34] H. Yu, G.-B. Liu, P. Gong, X. Xu, and W. Yao, Dirac cones and Dirac saddle points of bright excitons in monolayer transition metal dichalcogenides, Nat. Commun. **5**, 3876 (2014).

[35] H. Yu, X. Cui, X. Xu, and W. Yao, Valley excitons in two-dimensional semiconductors, Natl. Sci. Rev. **2**, 57 (2015).

[36] C. Robert, D. Lagarde, F. Cadiz, G. Wang, B. Lassagne, T. Amand, A. Balocchi, P. Renucci, S. Tongay, B. Urbaszek, and X. Marie, Exciton radiative lifetime in transition metal dichalcogenide monolayers, Phys. Rev. B **93**, 205423 (2016).

[37] M. Palummo, M. Bernardi, and J. C. Grossman, Exciton radiative lifetimes in two-dimensional transition metal dichalcogenides, Nano Lett. **15**, 2794 (2015).

[38] M. I. D'yakonov, V. A. Marushchak, V. I. Perel', and A. N. Titkov, The effect of strain on the spin relaxation of conduction electrons in III-V semiconductors, Zh. Eksp. Teor. Fiz. **60**, 1971 (1954) [Sov. Phys. JETP **63**, 655 (1986)].

[39] L. Wang and M. Wu, Intrinsic electron spin relaxation due to the D'yakonov–Perel' mechanism in monolayer MoS_2, Phys. Lett. A **378**, 1336 (2014).

[40] A. Rustagi and A. F. Kemper, Photoemission signature of excitons, Phys. Rev. B **97**, 235310 (2018).

[41] E. Perfetto, D. Sangalli, A. Marini, and G. Stefanucci, First-principles approach to excitons in time-resolved and angle-resolved photoemission spectra, Phys. Rev. B **94**, 245303 (2016).

[42] R. Wallauer, J. Reimann, N. Armbrust, J. Güdde, and U. Höfer, Intervalley scattering in MoS_2 imaged by two-photon photoemission with a high-harmonic probe, Appl. Phys. Lett. **109**, 162102 (2016).

[43] R. Wallauer, P. Marauhn, J. Reimann, S. Zoerb, F. Kraus, J. Güdde, M. Rohlfing, and U. Höfer, Momentum-resolved observation of ultrafast interlayer charge transfer between the topmost layers of MoS_2, Phys. Rev. B **102**, 125417 (2020).

[44] T. Rohwer, S. Hellmann, M. Wiesenmayer, C. Sohrt, A. Stange, B. Slomski, A. Carr, Y. Liu, L. M. Avila, M. Kalläne *et al.*, Collapse of long-range charge order tracked by time-resolved photoemission at high momenta, Nature (London) **471**, 490 (2011).

[45] D. Christiansen, M. Selig, E. Malic, R. Ernstorfer, and A. Knorr, Theory of exciton dynamics in time-resolved ARPES: Intra- and intervalley scattering in two-dimensional semiconductors, Phys. Rev. B **100**, 205401 (2019).

[46] H. Tanimura, K. Tanimura, and P. H. M. van Loosdrecht, Dynamics of incoherent exciton formation in Cu_2O: Time- and angle-resolved photoemission spectroscopy, Phys. Rev. B **100**, 115204 (2019).

[47] H. Tanimura and K. Tanimura, Momentum-resolved spectroscopy for the saddle-point excitons in InSb, Phys. Rev. B **102**, 235202 (2020).

[48] J. Madéo, M. K. L. Man, C. Sahoo, M. Campbell, V. Pareek, E. L. Wong, A. Al-Mahboob, N. S. Chan, A. Karmakar, B. M. K. Mariserla, X. Li, T. F. Heinz, T. Cao, and K. M. Dani, Directly visualizing the momentum-forbidden dark excitons and their dynamics in atomically thin semiconductors, Science **370**, 1199 (2020).

[49] R. Wallauer, R. Perea-Causin, L. Münster, S. Zajusch, S. Brem, J. Güdde, K. Tanimura, K.-Q. Lin, R. Huber, E. Malic, and U. Höfer, Momentum-resolved observation of exciton formation dynamics in monolayer WS_2, Nano Lett. **21**, 5867 (2021).

[50] W. Lee, Y. Lin, L.-S. Lu, W.-C. Chueh, M. Liu, X. Li, W.-H. Chang, R. A. Kaindl, and C.-K. Shih, Time-resolved ARPES determination of a quasi-particle band gap and hot electron dynamics in monolayer MoS_2, Nano Lett. **21**, 7363 (2021).

[51] J. Maklar, S. Dong, S. Beaulieu, T. Pincelli, M. Dendzik, Y. W. Windsor, R. P. Xian, M. Wolf, R. Ernstorfer, and L.

Rettig, A quantitative comparison of time-of-flight momentum microscopes and hemispherical analyzers for time- and angle-resolved photoemission spectroscopy experiments, Rev. Sci. Instrum. **91**, 123112 (2020).

[52] H. Hedayat, C. J. Sayers, A. Ceraso, J. van Wezel, S. R. Clark, C. Dallera, G. Cerullo, E. D. Como, and E. Carpene, Investigation of the non-equilibrium state of strongly correlated materials by complementary ultrafast spectroscopy techniques, New J. Phys. **23**, 033025 (2021).

[53] P. Hein, A. Stange, K. Hanff, L. X. Yang, G. Rohde, K. Rossnagel, and M. Bauer, Momentum-resolved hot electron dynamics at the $2H-MoS_2$ surface, Phys. Rev. B **94**, 205406 (2016).

[54] K. Hao, G. Moody, F. Wu, C. K. Dass, L. Xu, C.-H. Chen, L. Sun, M.-Y. Li, L.-J. Li, A. H. MacDonald *et al.*, Direct measurement of exciton valley coherence in monolayer WSe_2, Nat. Phys. **12**, 677 (2016).

[55] M. Schüler, T. Pincelli, S. Dong, T. P. Devereaux, M. Wolf, L. Rettig, R. Ernstorfer, and S. Beaulieu, Polarization-modulated angle-resolved photoemission spectroscopy: Toward circular dichroism without circular photons and Bloch wave-function reconstruction, Phys. Rev. X **12**, 011019 (2022).

[56] M. Schüler, U. D. Giovannini, H. Hübener, A. Rubio, M. A. Sentef, and P. Werner, Local Berry curvature signatures in dichroic angle-resolved photoelectron spectroscopy from two-dimensional materials, Sci. Adv. **6**, eaay2730 (2020).

[57] R. P. Day, B. Zwartsenberg, I. S. Elfimov, and A. Damascelli, Computational framework chinook for angle-resolved photoemission spectroscopy, npj Quantum Mater. **4**, 54 (2019).

[58] A. Kunin, S. Chernov, J. Bakalis, Z. Li, S. Cheng, Z. H. Withers, M. G. White, G. Schönhense, X. Du, R. K. Kawakami, and T. K. Allison, Momentum-resolved exciton coupling and valley polarization dynamics in monolayer WS_2, Phys. Rev. Lett. **130**, 046202 (2023).

[59] Time-reversal also implies $k_{zf} \to -k_{zf}$, so the "true" time-reversed pairs of final states are found on different sides of the TMD layer. The model predicts symmetric pocket profiles for escape from either side of a thin (1ML) suspended structure.

[60] A. Rustagi and A. F. Kemper, Coherent excitonic quantum beats in time-resolved photoemission measurements, Phys. Rev. B **99**, 125303 (2019).

[61] L. Guo, M. Wu, T. Cao, D. M. Monahan, Y.-H. Lee, S. G. Louie, and G. R. Fleming, Exchange-driven intravalley mixing of excitons in monolayer transition metal dichalcogenides, Nat. Phys. **15**, 228 (2019).

[62] One can choose the phase of $|B = c, v; \tau\rangle$ such that $\mathrm{Im}(\pi_\tau^2) = 0$.

[63] Y.-C. Wu, T. Taniguchi, K. Watanabe, and J. Yan, Enhancement of exciton valley polarization in monolayer MoS_2 induced by scattering, Phys. Rev. B **104**, L121408 (2021).

[64] Z. Wang, A. Molina-Sanchez, P. Altmann, D. Sangalli, D. De Fazio, G. Soavi, U. Sassi, F. Bottegoni, F. Ciccacci, M. Finazzi *et al.*, Intravalley spin–flip relaxation dynamics in single-layer WS_2, Nano Lett. **18**, 6882 (2018).

[65] S. Bae, K. Matsumoto, H. Raebiger, K.-i. Shudo, Y.-H. Kim, Ø. S. Handegård, T. Nagao, M. Kitajima, Y. Sakai, X. Zhang *et al.*, K-point longitudinal acoustic phonons are responsible for ultrafast intervalley scattering in monolayer $MoSe_2$, Nat. Commun. **13**, 4279 (2022).

[66] S. Brem, M. Selig, G. Berghaeuser, and E. Malic, Exciton relaxation cascade in two-dimensional transition metal dichalcogenides, Sci. Rep. **8**, 8238 (2018).

[67] S. Brem, A. Ekman, D. Christiansen, F. Katsch, M. Selig, C. Robert, X. Marie, B. Urbaszek, A. Knorr, and E. Malic, Phonon-assisted photoluminescence from indirect excitons in monolayers of transition-metal dichalcogenides, Nano Lett. **20**, 2849 (2020).